

Wideband Current Transducer for Measuring AC Signals With Limited DC Offset

Michael Hartmann, *Student Member, IEEE*, Juergen Biela, *Member, IEEE*, Hans Ertl, *Member, IEEE*, and Johann W. Kolar, *Senior Member, IEEE*

Abstract—In many applications, a current measurement that can measure ac currents with dc offset is required. This is not possible using conventional current transformers (CTs) due to the core saturation because of the dc offset. In this paper, a new sensor concept is presented, which consists of a wideband CT and a demagnetizing circuit. The sensor concept is capable of measuring ac currents with dc offset, which have periodic zero crossings, as given in power-factor-corrected (PFC) circuits. Using the demagnetization circuit, the core is actively reset during the zero crossing intervals. The operation principle and design equations are discussed in detail in this paper. For validating the presented concept, three sensors have been built using different core materials, and measurements of the transfer functions as well as operation in a PFC system are presented. A bandwidth from dc up to 20 MHz has been achieved.

Index Terms—Current measurement, current transformer (CT), nanocrystalline material.

I. INTRODUCTION

AN INCREASING number of power electronic systems connected to the power grid, such as input stages of telecom power supplies [1], [2], front-end systems of drives [3], or power electronics for renewable energy sources [4], [5], are realized with active rectifier circuit topologies. In order to minimize the influence on the mains, sinusoidal input currents and a unity power factor are required. A current controller is used to achieve these requirements, for which the input currents must be measured (cf., Fig. 1). Additionally, a superimposed voltage or load regulation is applied, which is not shown in Fig. 1 for simplicity. In contrast to single-phase systems with a typical power level below 1 kW, where often shunt resistors are used for current measurement, a galvanically isolated current measurement is required for higher power levels, where usually three-phase systems are utilized. Such a concept offers the advantage of lower losses, since usually no shunt resistors are used, and measurement signals that can be processed directly by the digital signal processor. Therefore, it is very important that the current sensor should also measure dc currents besides the ac component in order to guarantee dc-free mains currents.

Manuscript received August 29, 2008; revised November 28, 2008. Current version published July 29, 2009. Recommended for publication by Associate Editor C. R. Sullivan.

M. Hartmann, J. Biela, and J. W. Kolar are with the Power Electronic Systems Laboratory, Swiss Federal Institute of Technology (ETH) Zurich, CH-8092 Zurich, Switzerland (e-mail: hartmann@lem.ee.ethz.ch; biela@lem.ee.ethz.ch; kolar@lem.ee.ethz.ch).

H. Ertl is with the Power Electronics Section, Vienna University of Technology, A-1040 Vienna, Austria (e-mail: j.ertl@tuwien.ac.at).

Digital Object Identifier 10.1109/TPEL.2009.2017263

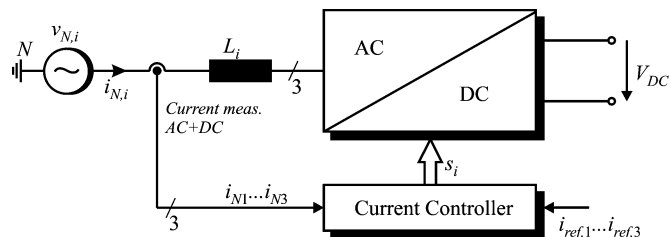


Fig. 1. AC/DC converter with sinusoidally controlled input currents. In order to guarantee dc-free input currents, a current sensor that can measure the ac and dc components of the input current has to be used.

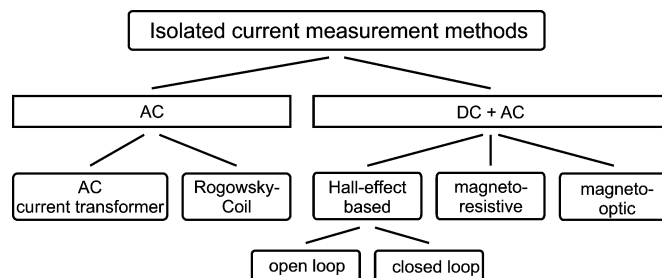


Fig. 2. Classification of isolated current measurement principles.

The general trend for higher power densities is driven by cost reduction, an increased functionality, and limited weight/space, in some applications (e.g., automotive and aircraft) [6]. This finally results in constantly increasing switching frequencies, which comes along with an increased bandwidth requirement for the current sensor. In particular, control strategies such as direct power control [7] or decoupled hysteresis control [8], [9], where the switching instants are directly derived from the measured currents, require exact knowledge of the current ripple. Also, in aircraft power supplies, which have very rigid requirements on the total harmonic distortion (THD < 3%), high bandwidth current sensors are necessary. This will be even more important in future aircraft systems, which will be based on ac voltages with variable frequency (360–800 Hz), resulting in switching frequencies of several 100 kHz [10].

In Fig. 2, a survey of available isolated current sensing methods is given. To measure pure ac currents, Rogowski coil transducers or ac current transformers (CTs) can be used. Because of the measurement principle, the Rogowski coil requires additional electronic circuitry, but can achieve a high bandwidth [11], [12]. AC CTs offer a wide bandwidth up to tens of megahertz and are widely used at higher current levels [13]. They are also suitable for analyzing switching transients of converters [14], [15]. The main limitation of this sensor type includes the core saturation at lower frequencies or the presence of a dc component.

DC and ac currents can be measured using Hall-effect-based sensors, transducers based on the magnetoresistive effect or for high voltage, and current levels by magneto-optic sensors. Optical current transducers [16] are based on the Faraday effect, and basically offer a wide bandwidth. Their main application areas are high-voltage power distribution systems. The essential drawbacks of this sensor type are its nonlinearity and the huge temperature dependency. Current sensors based on the magnetoresistive effect are commercially available for several years [17]. They are very attractive for integration in power electronic systems. However, the bandwidth of this sensor is limited to approximately 1 MHz due to the physical limitations of the magnetoresistive sensor element [18].

Hall effect current transducers are based on a Hall-type sensing device located in the air gap of a magnetic core to detect dc + ac components up to several 10 kHz. In closed-loop configuration, the Hall element is used to compensate the low-frequency flux in the core in combination with an amplifier feedback path. In open-loop configuration, the Hall device is used for sensing the current components directly, leading to a reduced linearity in comparison to a closed-loop sensor. Both configurations can be combined with a CT that has to be matched with the ac performance of the Hall element. This concept enables high-performance current sensors with a bandwidth from dc up to 30 MHz [19].

The Hall element has also been successfully combined with a Rogowski coil, which is also known as HOKA [20]. To insert the Hall element in the magnetic path, a core with an air gap is required, which may be a complex and expensive production step. Additionally, two sensor elements are needed for these transducer types. Furthermore, several systems have been reported to measure dc currents with an ac CT using the nonlinear magnetizing curve of the CT [21], [22]. Unfortunately, these concepts have a very limited upper bandwidth. Several other core flux cancellation techniques were reported in the literature [23], [24]; however, they show limited upper bandwidth and higher complexity. Pulse currents, as they occur in the switch or in the diode of a dc/dc converter, can be measured using a CT [25], if the CT is demagnetized periodically between the current pulses. As shown in [26], the system behavior of these circuits can be improved by replacing the burden resistance with an active stage (active loading) and applying synchronous rectification. In [27], additional reset voltage feedback is used to determine a necessary compensation voltage for the magnetic flux. If pulse current CTs are arranged in a dual transformer arrangement, such CTs can be used for inductor current measurements of a power-factor-corrected (PFC) stage [28]. However, two CTs are needed (one to sense the switch current and the other to sense the current through the boost diode) and their output signal has to be combined, which may be difficult in a practical realization.

Since the known concepts have limitations because of their bandwidth and/or requirement of complex core geometries or measurement electronics, a new and simple concept for ac and dc current measurement in active rectifier systems, which does not require additional sensor elements for detecting the magnetic flux, is proposed in this paper.

In the considered active rectifiers, the input currents have approximately a sinusoidal shape and therefore show zero crossings at fixed time intervals. Furthermore, the measurement signals of the input currents are only required during the positive/negative half-wave between the zero crossings. Therefore, the new sensor consists of a conventional CT, which does not saturate during the half-wave of the input current and measures the ac and dc components of the input current during this time. During the zero crossings, the current is kept for a short time at zero by the current controller, and the magnetic core can be reset/demagnetized so that the flux is zero at the beginning of the next half-wave and can measure the current during the next half-wave (cf., Fig. 3).

Since there are already distortions at the zero crossings of the input currents of a PFC, which can not be avoided completely [29], the short time for demagnetizing the current sensors does not cause noticeable additional distortion. Consequently, the CT in combination with minor extensions in the current controller can be used for measuring the ac as well as the dc components of the input current without any additional sensor element. Because the voltage does not need to be in phase with the input current, the proposed sensor concept is not limited to only PFC applications. The sensor concept requires that the current to be measured periodically gets zero for a certain time interval and can therefore be used in all applications where this requirement is fulfilled.

II. PRINCIPLE OF OPERATION

In Fig. 3(a), the schematic of the proposed current sensor for a single-phase PFC circuit is given, where the current sensor is located on the ac side of the active rectifier. Therefore, the current sensor using a CT consisting of a transformer and the burden resistance R_B is extended by the switch S_2 , two Zener diodes, and some control logic implemented in the (digital) current controller. If S_2 is closed, voltage $v_{i,\text{meas}}$ is equal to the voltage across the burden resistor, which is proportional to the input current: $v_{i,\text{meas}} = i_N/N R_B$. As shown in Fig. 3(b), the magnetizing current i_m of the CT raises during the half-wave of the input current (details are discussed in the following section). If a sinusoidal current i_N causing a sinusoidal voltage $v_{i,\text{meas}}$ is assumed, the magnetizing current at instant $T/2$ can be calculated approximately by

$$i_m = \frac{R_B}{L_m} \int_0^{T/2} \frac{\hat{I}_N}{N} \sin(\omega\tau) d\tau = \frac{2\hat{I}_N R_B}{L_m N \omega}. \quad (1)$$

In case of a purely sinusoidal current i_N , the magnetizing current i_m will be zero after a full period T . In Fig. 3(b), a small dc component is assumed, hence a small value of i_m will remain after one period T . Without any demagnetizing, i_m would raise more and more in case the input current has a dc component, and the core of the CT would saturate after some period.

By demagnetizing the CT at each zero crossing of the primary current, the dc component does not lead to a core saturation, which can be measured by comparing the positive and negative half-wave. For demagnetizing the core, the zero crossing of i_N is detected, and the pulsewidth modulation (PWM) signal of the

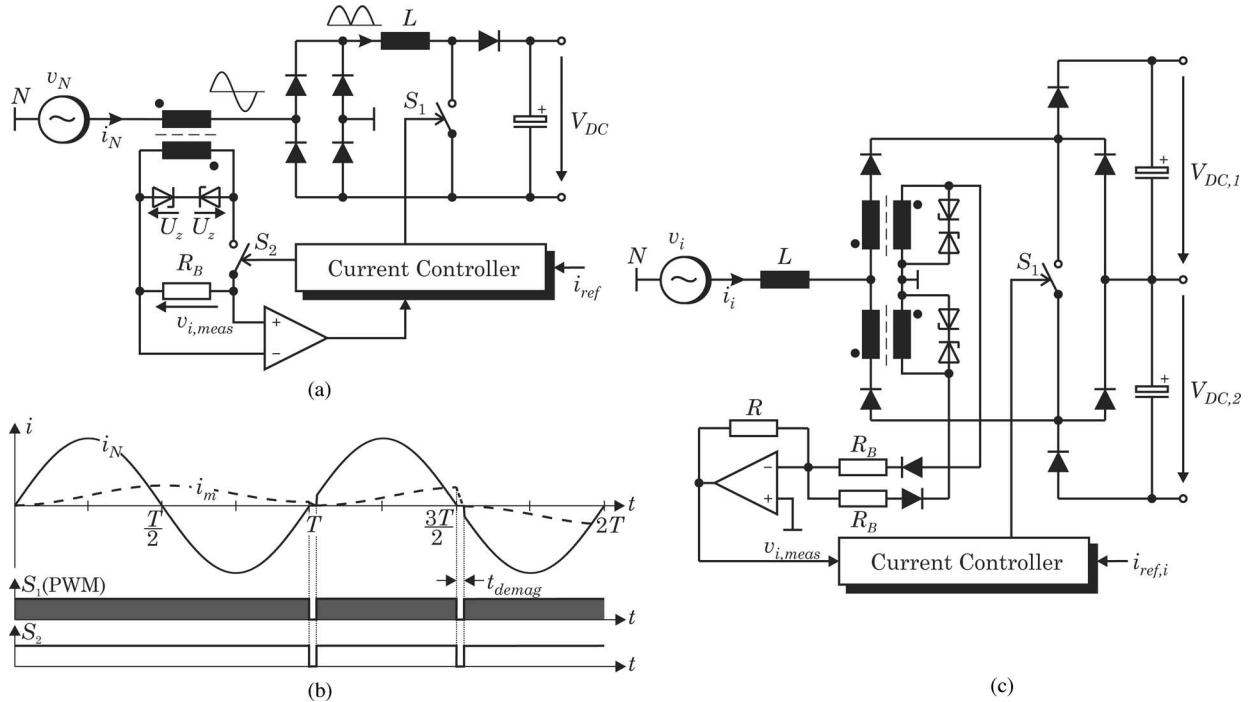


Fig. 3. Schematic of the proposed current sensor consisting of a CT and a demagnetizing circuit for (a) a single-phase PFC. (b) Demagnetization concept with demagnetization after a full period and after a half-period. (c) One phaseleg of the realization for a three-phase active rectifier (for example, a VIENNA rectifier circuit is shown).

PFC switch S_1 is set to zero, so that the primary current of the CT stays zero. At the same time, S_2 is opened ($v_{i,meas}$ is held to zero by the burden resistor R_B) and the magnetizing current of the CT now flows via the Zener diodes. Since the Zener voltage of the diodes is much higher than the magnitude of $v_{i,meas}$, the time to demagnetize the core is very short. After the CT is fully demagnetized, S_2 can be closed and the PWM signal generated from the current controller is reapplied to S_1 . The time needed to demagnetize the current sensor t_{demag} can be calculated easily using the approximation

$$U_z = L_m \frac{di_m}{dt} \approx L_m \frac{\Delta i_m}{\Delta t} \quad (2)$$

which leads to

$$t_{demag} = \frac{R_B}{NU_z} \int_0^{t_{meas}} i_N(\tau) d\tau \quad (3)$$

where t_{meas} denotes the measuring time until the sensor is demagnetized. As the phase current of the rectifier is forced to zero during t_{demag} , the sensor concept causes current distortions in the input current i_N . Since several other effects, such as cusp distortion [30] or discontinuous-mode (DCM) of operation of the boost inductor [31], already generate zero crossing distortions, the distortions caused by the proposed sensor concept are not significant. In Fig. 4, the harmonics of an average current-mode-controlled 1-kW single-phase PFC prototype with and without the new sensor concept are shown. As it can be seen, no noticeable additional harmonics are caused by the demagnetizing circuit. In applications where no nameable current distortion occurs, such as bidirectional rectifiers or situations where a phase shift is included between voltage and current, the time

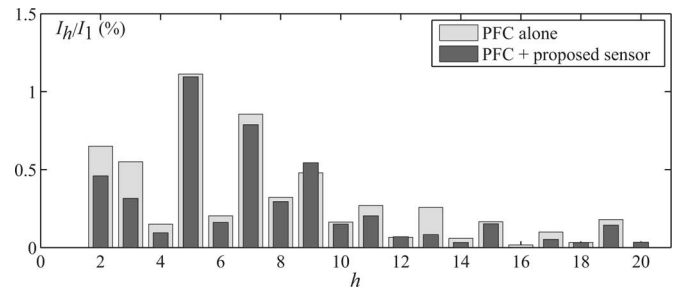


Fig. 4. Current harmonics of the PFC and the PFC in combination with the proposed sensor concept. Measurements are taken from an average current-mode-controlled 1-kW PFC prototype.

interval needed for demagnetizing the CT will result zero crossing distortions. The amount of these distortions depends on the sensor realization, but generally should not be higher than the distortions given in Fig. 4.

The demagnetization of the CT core can also be done every half-period, which is shown in Fig. 3(b) for $t > T$. This is very useful, if the sensor is located on the dc side of the rectifier [Fig. 18(c)], since the current to be measured includes a significant dc component, as illustrated in Fig. 3(a). In order to retain a small core size, the CT must then be demagnetized every half period of the mains.

In Fig. 3(c), the proposed sensor concept is applied to a phaseleg of a Vienna rectifier structure. Here, two CTs are used and one CT is placed in each diode path, which only conducts for half a period. No additional switch is required here as the time interval with zero current is inherently used for demagnetization.

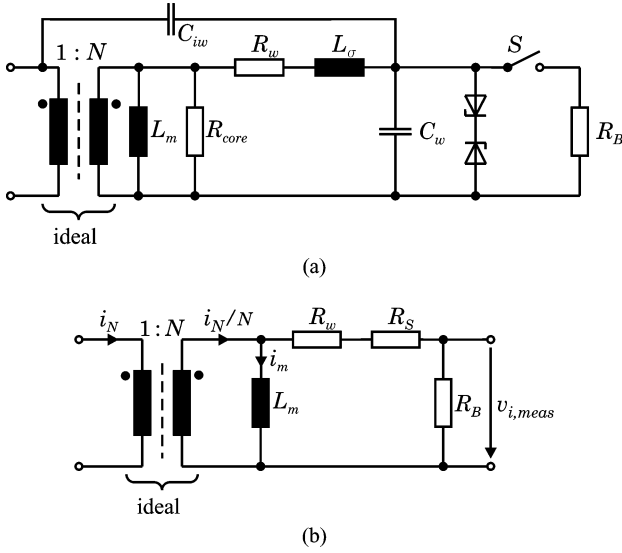


Fig. 5. Equivalent circuits of the CT with demagnetizing circuit including (a) parasitic elements and (b) low-frequency equivalent circuit for closed switch S_2 .

A. Model of the Current Transformer

In order to be able to design and optimize the current sensor, a model of the CT is required. The detailed model of the current sensor is given in Fig. 5, where the following symbols are used:

- L_m : magnetizing inductance
- R_{core} : equivalent resistor for core losses
- L_σ : leakage inductance
- R_w : winding resistance
- C_w : winding capacitance
- C_{iw} : capacitance between primary and secondary winding
- N : number of turns
- R_B : burden resistance
- R_S : on-resistance of the switch.

The CT is modeled by an ideal transformer with a single-turn primary winding and an N -turn winding on the secondary side. The nonideal behavior of the sensor is modeled by the network located at the secondary side of the ideal transformer. For analyzing the sensor's low-frequency and high-frequency behavior, simplified/adapted models as shown in Figs. 5(b) and 7 are used.

1) *Low-Frequency Behavior*: For analyzing the low-frequency behavior of the sensor, the interwinding capacitance C_{iw} , the leakage inductance L_σ , the winding capacitance C_w , and the core losses, represented by R_{core} , can be neglected [Fig. 5(b)].

In a first approximation, the lower cutoff frequency f_l of the current sensor can be calculated by

$$f_l = \frac{R}{2\pi L_m} \quad (4)$$

where R is the sum of the resistors $R = R_w + R_s + R_B$ [cf., Fig. 5(b)]. Since the CT is demagnetized every half-period, the sinusoidal steady-state condition is not given, so that the

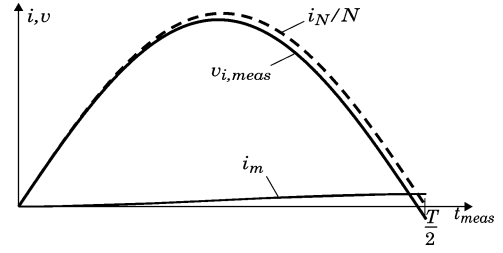


Fig. 6. Deviation of the sensor output $v_{i, meas}(t)$ from the current $i_N(t)/N$ ($i_N(t)$ transferred to the secondary side), caused by the magnetizing current $i_m(t)$ for a CT with $L_m = 200$ mH and $R_B = 1.2 \Omega$.

differential equation for the magnetizing current

$$\frac{L_m}{R} \frac{di_m(t)}{dt} + i_m(t) = \frac{i_N(t)}{N} \quad (5)$$

must be solved. For a sinusoidal primary current $i_N = \hat{I}_N \sin(\omega t)$, the solution of (5) is given by

$$i_m(t) = K(\omega L_m e^{(R/L_m)t}) - \omega L_m \cos(\omega t) + R \sin(\omega t) \quad (6)$$

using

$$K = \frac{\hat{I}_N R}{N(R^2 + \omega^2 L_m^2)}.$$

Using $i_m(t)$, the output voltage of the sensor results

$$v_{i, meas}(t) = R_B \left(\frac{\hat{I}_N}{N} \sin(\omega t) - i_m(t) \right). \quad (7)$$

Here, it can be seen that $v_{i, meas}(t)$ not only depends on the input current, but also on the magnetizing current, which results in measurement errors. In Fig. 6, $v_{i, meas}(t)$ and $i_m(t)$ are plotted for the values $L_m = 200$ mH, $R_B = 1.2 \Omega$. To minimize this error, L_m should be as large as possible. For the PFC application, this error results in a measurement signal that represents a too small rms value of the measured current. A superimposed voltage or power controller, however, will automatically compensate this effect. The deviation can also be easily calculated if L_m and R_w are known, which allows a compensation based on a feed forward of the current controller.

In order to quantify this deviation, an error function

$$\text{err} = \left(\frac{|v_{i, meas}(t = T/2)|}{\hat{I}_N/N} \right) 100\% \quad (8)$$

can be defined. Additionally, a THD calculation can be used to quantify the resulting distortion of the measurement signal.

2) *HF Behavior*: In contrast to the low-frequency model, the parasitic elements of the CT cannot be neglected for the HF behavior. Additionally, the parasitic inductance L_B of the burden resistance R_B and the junction capacitance C_d of the diodes have to be considered. Basically, the winding-to-winding and the core-to-winding capacitors are distributed, which are difficult to model. In a first approximation, these capacitors can be approximated by six independent capacitors, as described in [32]. This model is valid up to frequencies between the first and the second resonance of the transformer. For the following,

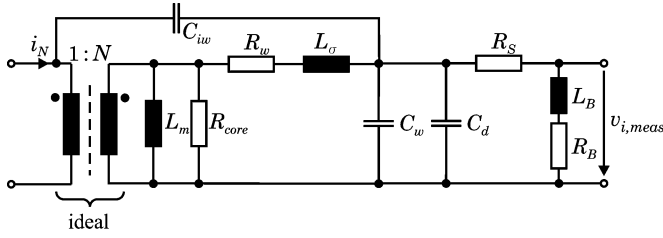


Fig. 7. HF equivalent circuit of the current sensor.

the six capacitors are reduced to the winding capacitance C_w and the interwinding capacitance C_{iw} , which describe the relevant influence of the capacitors on the transfer function of the current sensor, with a sufficient accuracy. The calculation of the upper frequency limit poses a real challenge. To get good results, the frequency dependency of the core material [33] and a more distributed model, as it is shown in [34], has to be considered. Here, a finite-element method (FEM) simulation is used to determine the distributed elements. In general, the upper bandwidth limit of the CT is given by a parallel resonance circuit of C_w , L_σ , and/or L_m . So it is essential to keep the winding capacitance C_w as small as possible. C_w can be minimized using a single-layer winding strategy for this, and is mainly determined by the winding-to-core capacitance [35]. Fortunately, this parallel resonance circuit is damped by the burden resistance R_B , which is, in the desired application, typically small compared to the natural impedance Z_0 of the resonance circuit. Therefore, the upper bandwidth can be further increased if C_w is minimized, and can be calculated by the more distributed model [35].

However, some design rules can be derived from the HF model of Fig. 7. In order to get the highest possible upper bandwidth, a single-layer winding strategy and, since C_w is proportional to N , a minimum number of turns have to be used.

B. Dimensioning of the Magnetic Core

The core size and the number of turns N of the CT have to be chosen so that the magnetic core does not saturate for the lowest occurring frequency $f_{\min} = \omega_{\min}/(2\pi)$. Using Faraday's law and neglecting the on-resistance R_S of the switch results in

$$\int_0^{t_{\text{meas}}} \frac{i_N(t)}{N} (R_B + R_w) dt = N (B_{\text{sat}} - B_r) A_{fe} \quad (9)$$

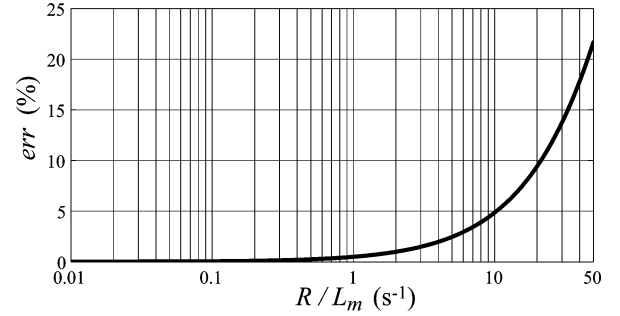
where B_{sat} is the saturation induction, B_r the remanence, and A_{fe} the cross-sectional area of the core.

For a sinusoidal primary current and demagnetization after each half-period, the left-hand side of (9) can be used to determine N

$$\begin{aligned} \int_0^{T/2} \frac{\hat{I}_N}{N} \sin(\omega_{\min} t) (R_B + R_w) dt \\ = KL_m^2 \omega_{\min} \left(1 + e^{\pi R/\omega_{\min} L_m}\right). \end{aligned} \quad (10)$$

Here, the inductance

$$L_m = N^2 A_L \quad (11)$$

Fig. 8. Error of the approximation given in (13) as a function of R/L_m .

is also expressed as function of N . This results in

$$\begin{aligned} \frac{R \hat{I}_N \omega_{\min} (N^2 A_L)^2}{N (R^2 + (\omega_{\min} N^2 A_L)^2)} \left(1 + e^{\pi R/\omega_{\min} N^2 A_L}\right) \\ = N (B_{\text{sat}} - B_r) A_{fe}. \end{aligned} \quad (12)$$

Since (12) cannot be solved analytically, either a numerical solution or an approximation has to be used. If the influence of i_m is neglected to determine N

$$\begin{aligned} \int_0^{T/2} R \left(\frac{\hat{I}_N}{N} \sin(\omega_{\min} t) - i_m(t) \right) dt \\ \approx \int_0^{T/2} R \frac{\hat{I}_N}{N} \sin(\omega_{\min} t) dt = \frac{2R \hat{I}_N}{N \omega_{\min}} \end{aligned} \quad (13)$$

is valid, and (12) simplifies to

$$\frac{2R \hat{I}_N}{N \omega_{\min}} (R_B + R_w) = N (B_{\text{sat}} - B_r) A_{fe} \quad (14)$$

which can be solved analytically. The error caused by this simplification is depicted in Fig. 8. It can be seen that the approximation shows good results for $R/L_m < 10 \text{ s}^{-1}$.

With the desired sensitivity

$$S = \frac{v_{i,\text{meas}}}{i_N} = \frac{R_B}{N} \rightarrow R_B = SN \quad (15)$$

the burden resistance can also be expressed as function of N . Furthermore, the winding resistance

$$R_w = \frac{\sqrt{2} J l_m}{\hat{I}_N \gamma_{\text{cu}}} N^2 \quad (16)$$

is a function of N , where J denominates the desired current density, l_m the medium turn length, and γ_{cu} the conductivity of the wire.

Combining (14), (15), and (16) results in an equation for determining the minimum number of windings

$$N_{\min} = \frac{S \hat{I}_N}{\omega_{\min} A_{fe} (B_{\text{sat}} - B_r) - (\sqrt{2} l_m J / \gamma_{\text{cu}})} \quad (17)$$

so that the core does not saturate. The validity of this result has to be checked using Fig. 8.

This results does not give any information about the amplitude error of the sensor output. For limiting the amplitude error given by (8), the number of turns might have to be increased.

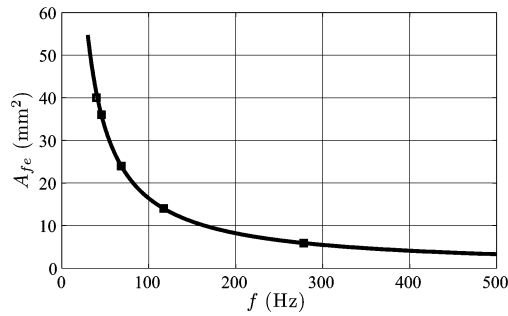


Fig. 9. Necessary core area A_{fe} as a function of the minimum frequency f_{min} [parameters: $N = 66$, $R_B = 0.66 \Omega$, and $\hat{I}_N = 25$ A, material: VP500F2 (also see Table II)].

According to (17), the core size A_{fe} of the CT can be reduced if the minimal frequency f_{min} is increased (e.g., 360–800 Hz in aerospace applications). In Fig. 9, the required core sizes for the nanocrystalline materials (see Section IV) are marked. The sensitivity S , the burden resistance R_B , and the number of turns are constant parameters. It can be seen that for a minimal frequency of $f_{min} = 400$ Hz, only one-sixth of the core area is needed, which makes the sensor type ideally suited for the aerospace applications. Also, another advantage of the CT can be derived from (17) using (15). For higher current levels, the same core size can be used, if R_B is reduced in the same manner as \hat{I}_N is increased. Here, it is important to note that for small values of R_B , the winding resistance must be considered, in order to limit the error caused by the voltage divider R_w/R_B .

III. APPLICATION OF A COMMERCIAL AC CURRENT TRANSFORMER

In a first step, the applicability of a commercial ac CT in the proposed current sensor concept is analyzed in the following. Here, the ac-CT ZKB 564/401-80 from Vacuumschmelze Corporation [36], designed for 50 Hz applications, is considered. In Table I, the main characteristics of the sensor are summarized. The secondary winding consists of $N = 1300$ turns, in order to achieve the 50 Hz capability. This results in a relatively large winding capacitance, which considerably reduces the HF performance of the sensor. The measured transimpedance transfer function of the sensor $G(j\omega) = v_{i,meas}(j\omega)/i_N(j\omega)$ has been recorded using a Bode100 network analyzer [37] [Fig. 10(a)]. Because of the large burden resistance (necessary for achieving the desired sensitivity of 50 mV/A), the 50 Hz phase shift is too large for the intended application. The active current probe TEK A6302 [38], which is able to measure continuous currents up to 20 A, will be used as reference in this paper. In this, current probe ac currents up to 100 MHz are sensed by a CT whose dc components, however, are compensated using a Hall device flux sensor in connection with an external amplifier module [39] in a closed-loop manner. This compensating (“MMF balance”) measuring principle, therefore, combines the high bandwidth of a conventional ac CT and of a dc capable (low frequency) Hall sensor avoiding linearity errors to a large extend. Additionally,

TABLE I
CHARACTERISTICS OF THE 50-Hz CAPABLE COMMERCIAL AC-CT ZKB 564/401-80

Size	32 × 16 × 32 mm
Nominal current	25 A _{eff}
Number of turns	1:1300
Burden resistance	65 Ω
Sensitivity	50 mV/A
Bandwidth	30 Hz...200 kHz

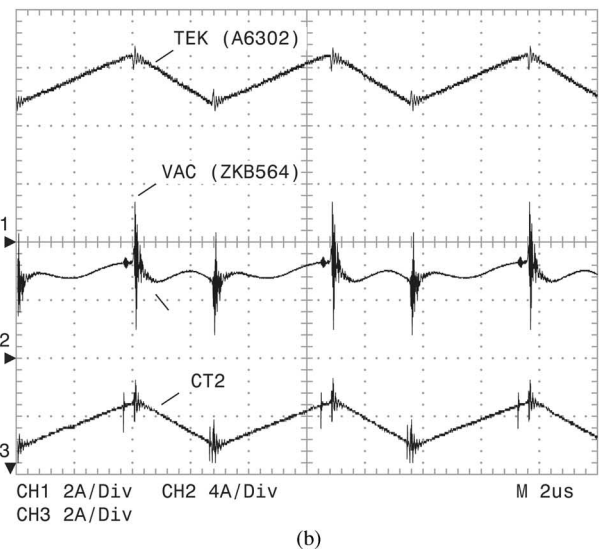
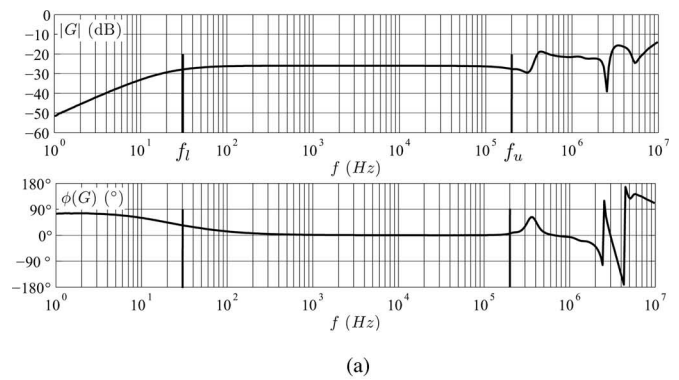


Fig. 10. Inductorcurrent measurement results of the commercial CT ZKB 564/401-80 of VAC. (a) Bode plot of the transimpedance gain $G(j\omega) = v_{i,meas}(j\omega)/i_N(j\omega)$. (b) Output voltage $v_{i,meas}$ taken from the 1-kW PFC circuit with a switching frequency of $f_s = 150$ kHz compared to the measuring results of a current clamp TEK (A6302) and the output voltage of realization CT2.

the A6302 is characterized by a high dv/dt immunity, which is achieved by carefully shielding and CM reduction measures.

The output signal of the current sensor, taken from the 1-kW PFC prototype with a switching frequency of 150 kHz, is compared with the output signal of the current probe TEK A6302 [cf., Fig. 10(b)]. The upper bandwidth is ≈ 200 kHz. Hence, the VAC CT cannot be used in the proposed sensor for measuring the current ripple of converters with medium or high switching frequencies. Therefore, a new CT is designed in the

TABLE II
SPECIFICATIONS OF THE MAGNETIC MATERIALS

	VP500F ₁	VP500F ₂	T ₃₈
B_{sat}	1.2 T	1.2 T	0.43 T
$B_{m,lin}$	1 T	1 T	0.3 T
B_r	0.3 T	0.05 T	0.05 T
$\mu_{r,i}$	≈ 100000	≈ 30000	10000
Curie temperature	$>600^\circ\text{C}$	$>600^\circ\text{C}$	$>130^\circ\text{C}$

following section, and the performance of the designed sensor is plotted in Fig. 10(b).

IV. DESIGN OF A HIGH-BANDWIDTH CT

As the commercial CTs are not appropriate for the proposed current sensor (cf., Section III), a CT with the following properties is designed.

- 1) 50-Hz capability and small amplitude error, as calculated in (8).
- 2) High upper cutoff frequency f_u .
- 3) Small size of the sensor.
- 4) Good sensitivity S .

To achieve a small amplitude error at 50 Hz, the magnetizing inductance L_m has to be large, which requires either a high-permeability core or a large number of turns N . Unfortunately, both measures reduce the upper bandwidth limit, so a tradeoff has to be found between the 50-Hz amplitude error and the upper bandwidth limit.

A. Magnetic Materials

For the CT design, the MnZn-ferrite T₃₈ and the two nanocrystalline materials VITROPERM 500F₁ (VP500F₁) as well as VITROPERM 500F₂ (VP500F₂) are compared. Their properties are given in Table II. Also, amorphous materials are appropriate for the design of a CT. However, the performance of the nanocrystalline materials surpasses the amorphous ones, only the nanocrystalline ones are considered in the following.

The two nanocrystalline materials offer the advantage of a very high saturation flux density of $B_{sat} = 1.2$ T and show a highly linear B-H characteristic up to $B_{m,lin} = 1$ T. Consequently, the core size of the CT with nanocrystalline material can be reduced compared to the MnZn-ferrite material T₃₈, which has just a saturation flux density of $B_{sat} = 0.43$ T. The measured hysteresis loops of the materials are plotted in Fig. 11(a). As depicted in Fig. 11(b), the initial permeability $\mu_{r,i}$ is also very high for the nanocrystalline materials. The material VP500F₁ offers a permeability of $\mu_{r,i} \approx 100000$ and seems to be best-suited. Unfortunately, this high-permeability material also has a very high remanence of $B_r = 0.3$ T [cf., Fig. 11(a)], which reduces the actually applicable amplitude range of the flux density. For the two other materials (with lower $\mu_{r,i}$), the influence of remanence can be neglected. Because of eddy currents, the complex permeability decreases for higher frequencies that must be considered when determining the sensor's HF behavior. The nanocrystalline materials show a very small temperature dependence of B_{sat} and μ_r . Additionally, the high Curie temperature

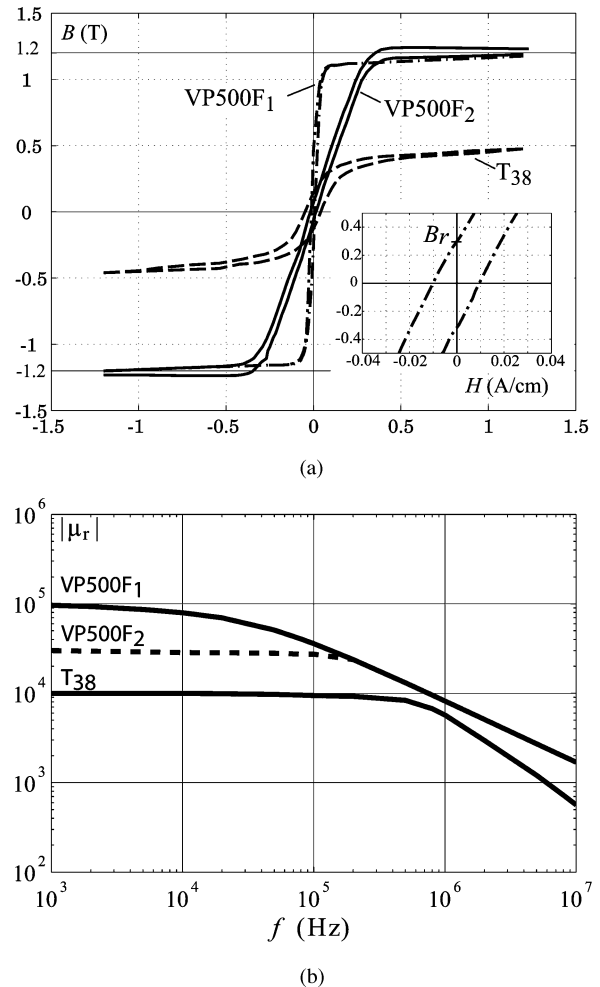


Fig. 11. (a) Measured hysteresis loop and (b) complex permeability $|\mu_r|$ as a function of the frequency f of the magnetic materials.

of more than 600°C allows a higher operating temperature of the core, making these materials suitable for power electronic applications.

B. Current Transformer Design

Using the considered materials, CTs for a sinusoidal primary current of $\pm 25\text{A}_{pk}$ (resulting in a dc component of $i_{avg} = (2/\pi)\hat{I} = 15.9$ A) and a frequency of 50 Hz have been designed, where the CT is assumed to be demagnetized every half-period. The characteristics of the three CTs are summarized in Table III. As the permeability of the ferrite material used for CT3 is much smaller, a bigger core size has to be applied. Equation (17) has been used for determining the minimum number of turns in order to avoid saturation. Since only the core saturation is considered in (17), the amplitude error of the CT [cf., (8) and the resulting THD (only distortions caused by the demagnetizing concept are considered) have been calculated for dependency on N (cf., Fig. 13 and Table III).

The amplitude error is reduced by increasing N , which, however, is limited due to the parasitic winding capacitance and the available core window. For the given case, it is not possible to

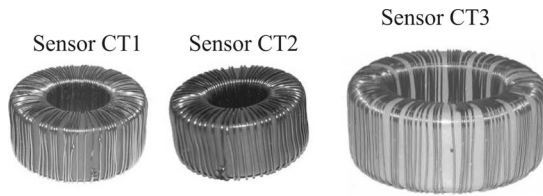


Fig. 12. Realized CTs. Sensor CT1 and CT2 use a nanocrystalline material and therefore a smaller core size is possible compared to sensor CT3 with the ferrite-material T₃₈.

TABLE III
CHARACTERISTICS OF THE DESIGNED CURRENT TRANSFORMERS

	Sensor CT1	Sensor CT2	Sensor CT3
Size	25×16×12 mm	25×16×12 mm	34×20.5×12.5 mm
Material	VP500F ₁	VP500F ₂	T ₃₈
N_{min}	105 turns	65 turns	119 turns
N_{used}	110 turns	66 turns	120 turns
L_m (50 Hz)	1.15 H	90 mH	170 mH
R_w	0.78 Ω	0.31 Ω	1.1 Ω
L_σ	728 μH	320 μH	1.1 mH
C_w	7 pF	7.5 pF	21 pF
R_B	1.1 Ω	0.66 Ω	1.2 Ω
S	10 mV/A	10 mV/A	10 mV/A
err (%)	1.3 %	6.1 %	6.5 %
THD (%)	0.6 %	2.1 %	2.2 %

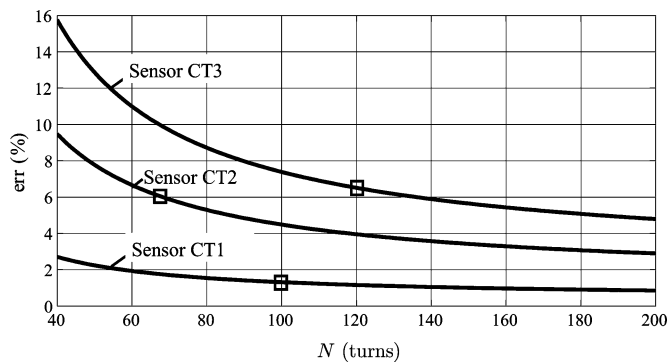


Fig. 13. Amplitude error according to (8) as a function of N . The realized number of turns are marked with a small square.

reduce the error below 2% for CT2 and CT3. For a further reduction of the error, a material with a higher permeability, for example, VP500F₁, must be used. Sensor CT1 uses the material with highest permeability and shows a small amplitude error at 50 Hz. Whereas, CT2 is more suited to achieve a high upper cutoff frequency.

In Fig. 14, the measured transimpedance transfer functions $G(j\omega)$ of the sensors are plotted. The upper bandwidth limit has to be defined either by the phase error or by the amplitude error of the CT. For CT2, both limitations result in an upper frequency limit of 20 MHz. So, a wideband CT from 50 Hz up to 20 MHz has been realized based on the nanocrystalline materials. Also, CT3 (using the ferrite material T₃₈) shows good, but slightly reduced performance results. For testing the HF behavior of the sensors, an (damped) oscillating current showing a frequency of about 3 MHz was applied to the primary side.

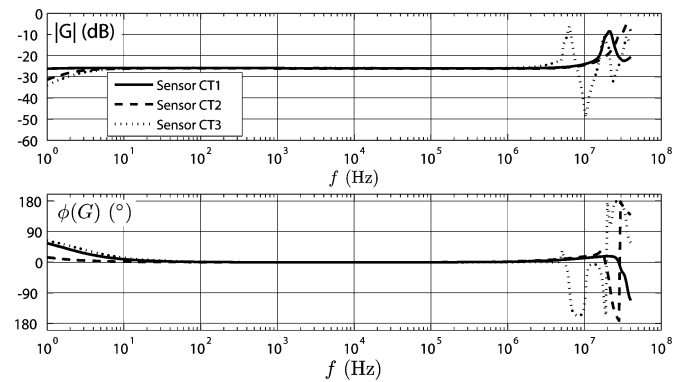


Fig. 14. Bodeplot of the transimpedance gain $G(j\omega) = v_{i, meas}(j\omega) / i_N(j\omega)$ of the three sensors.

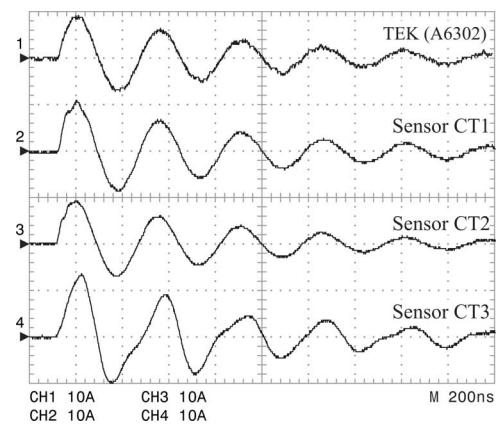


Fig. 15. Currentsensor outputs, measuring a 3 MHz/10 A ringing current.

The results, compared with the measurement of an active TEK A6302 current probe, are given in Fig. 15. Sensor CT2, which has the highest bandwidth, exhibits only a negligible deviation, whereas in the signals of CT1 and CT3, the bandwidth limitation become visible.

C. dv/dt Immunity Test

In many power electronic applications, a high dv/dt immunity is very important in order to limit the noise in the measurement signal. With a high dv/dt , the primary side of the CT couples to the secondary side via the interwinding capacitance C_{iw} of the sensor (cf., Fig. 7). A high dv/dt is, for example, generated by the switching transient of a MOSFET.

For testing the dv/dt immunity of the sensors, a boost-type converter circuit with switching transients of 15 kV/μs has been used. A stub line was connected to the drain of the MOSFET and was fed through the CT as primary conductor, where no current is flowing. Without any shielding, a relatively large noise signal of 2 A_{pk} is coupled to the secondary side [cf., Fig. 16(a)].

The noise can be reduced by shielding the primary inductor [cf., Fig. 16(b)]. Since the secondary winding of the CT is also coupled to the surrounded elements, a noticeable disturbance is still measured as compared to the results of the TEK A6302 current probe [cf., Fig. 16(c)]. A further improvement of the

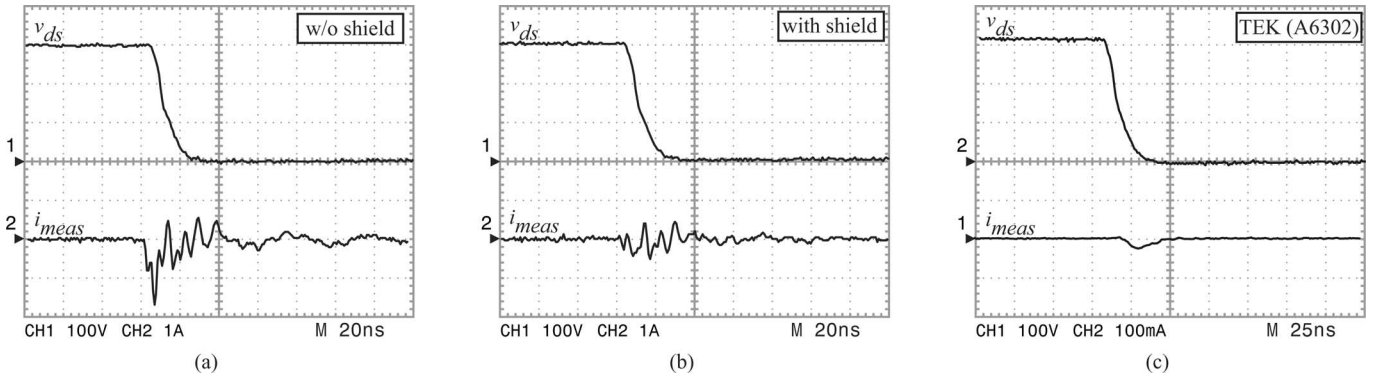


Fig. 16. dv/dt immunity test of CT1; voltage slope: $15 \text{ kV}/\mu\text{s}$, CH1: $v_{DS} \dots 100 \text{ V/Div}$, time scale: 20 ns/Div . (a) Measurement without shielding: $i_{meas} \dots 1 \text{ A/Div}$. (b) Measurement with primary conductor shielded: $i_{meas} \dots 1 \text{ A/Div}$. (c) TEK A6302 current probe as reference: $i_{meas} \dots 100 \text{ mA/Div}$.

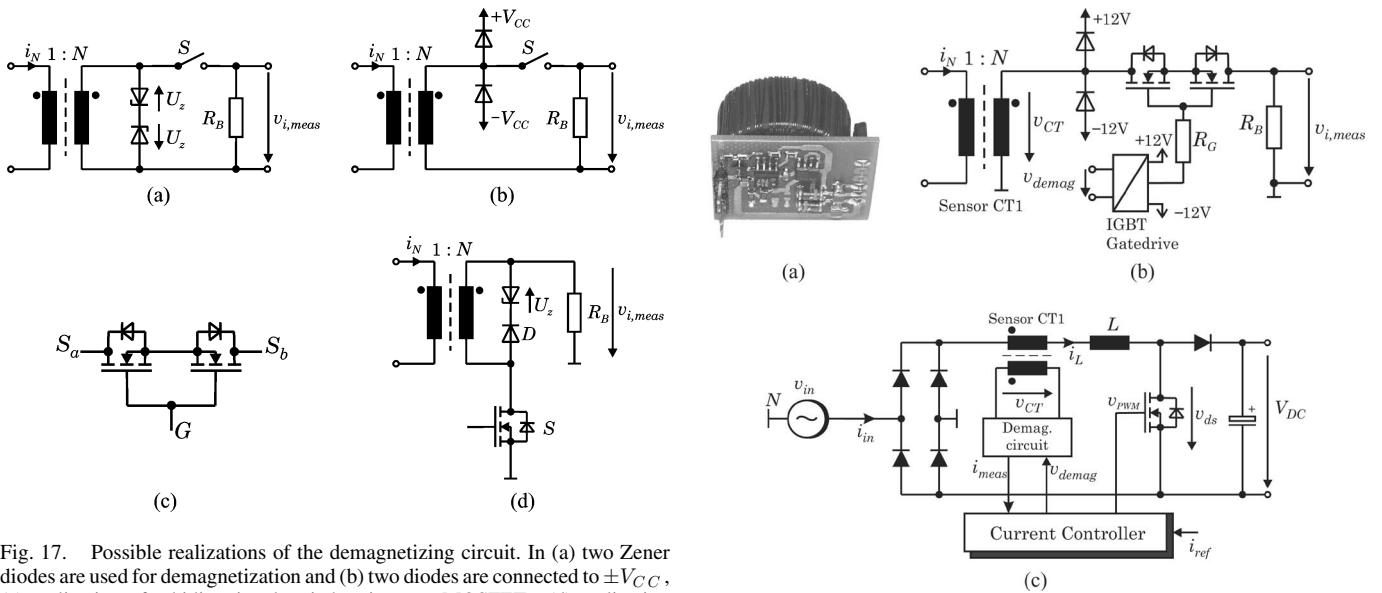


Fig. 17. Possible realizations of the demagnetizing circuit. In (a) two Zener diodes are used for demagnetization and (b) two diodes are connected to $\pm V_{CC}$, (c) realization of a bidirectional switch using two MOSFETs, (d) realization using just one MOSFET, if the sensor is placed on the dc side of the converter.

Fig. 18. Realized prototype to test the behavior of the proposed current sensor concept. (a) Picture of the sensor. (b) Schematic of the demagnetizing circuit. (c) PFC prototype (1 kW) where the sensor is located on the dc side of the converter.

dv/dt would require shielding of the entire CT and insertion of a small common-mode choke at the output of the winding [13].

V. DEMAGNETIZATION CIRCUIT

Several configurations of the demagnetizing circuits are possible in practice, which differ if the sensor is located on the ac side or on the dc side of the rectifier. In Fig. 17(a), for example, a demagnetizing circuit using two Zener diodes is shown. If a bipolar power supply (e.g., $\pm 12 \text{ V}$) is available, two diodes connected to the power supply, as shown in Fig. 17(b), can also be used. If the sensor is located on the ac side of the converter, a bidirectional realization of the switch S_2 is required. In the case of not too high-burden currents, integrated bidirectional analog switches may be used for realizing S_2 . Such analog switches offer a typical on-resistance of about $250 \text{ m}\Omega$ and a current capability up to 500 mA . However, for the designed CTs in Section IV, higher burden currents occur. Hence, a bidirectional switch arrangement, as shown in Fig. 17(c), is recommended. If the sensor is located on the dc side of the converter, a realization

using a single MOSFET is possible [cf., Fig. 17(d)]. For this realization also, only a single-clamp diode is necessary.

The realized prototype (cf., Fig. 18) uses the designed sensor CT1, and is based on the proposed bidirectional switch configuration of Fig. 17(c). The two MOSFETs are realized by the dual N-channel MOSFET IRF9956. This MOSFET shows a small output capacitance C_{oss} and a sufficient low $R_{DS,on}$. The gate drive is realized by an insulated-gate bipolar transistor (IGBT) gate drive optocoupler HCPL0314, which is fast enough and offers the capability of a bipolar output (see Section VI).

VI. EXPERIMENTAL RESULTS

For determining the performance of the prototype of the current sensor (cf., Fig. 18) a single-phase 1-kW PFC circuit has been utilized. The sensor prototype designed in Section V is located on the dc side of the PFC. As already mentioned, the primary current of the sensor (here, the inductor current i_L of

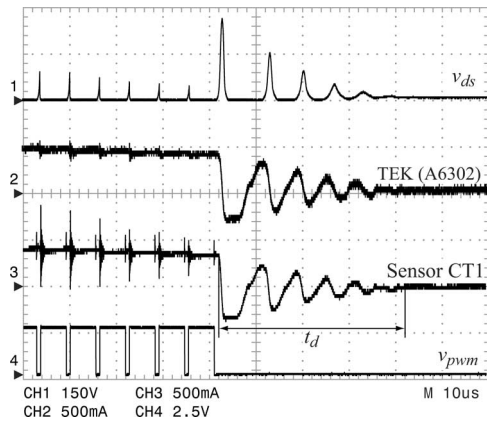


Fig. 19. Measurement taken from the PFC prototype at the zero crossing interval using the proposed sensor demagnetization scheme. Drain–source voltage v_{DS} of the PFC switch, inductor currents measured with the TEK A6302 current probe and sensor CT1. Additionally, the PWM signal of the PFC switch is shown. Because of the missing shielding of the CT, the sensor output of CT1 shows some ringing as compared to the current clamp, which is induced by the high dv/dt rates at the switching instants of the PFC switch (also see Fig. 16).

the PFC) has to be forced to zero by the current controller during the demagnetizing interval.

In a practical PFC realization, the current controller is not able to adjust an inductor current of zero because of Cusp distortion and DCM operation of the converter. Consequently, the input voltage v_{in} has to be used to detect the zero crossing to start the demagnetizing process. (The controller ensures nearly unity power factor.) However, if the PWM signal v_{PWM} of the MOSFET is forced to zero, the output capacitance C_{OSS} of the MOSFET builds a series resonant circuit together with the boost inductance L , which is excited by the inductor current i_L . Hence, a damped oscillation of the primary sensor current occurs (cf., Fig. 19). This can also be seen in the drain-to-source voltage v_{DS} , which is charged/recharged by this oscillating current. Additionally, it can be seen in the measurements that are near the zero crossings (where the inductor current is low), the drain–source voltage of the MOSFET does not rise up to the dc link voltage since the current is too small to charge the output capacitance of the MOSFET.

During the mentioned oscillation interval, the CT should not be demagnetized, because during demagnetization, a comparably high voltage (e.g., 12 V) is connected to the CT instead of the small burden resistance R_B , and this high voltage would rapidly increase the magnetizing current. Therefore, a delay has to be inserted between forcing the PWM signal to zero and demagnetizing. For the realized prototype, a necessary delay of $t_d = 40 \mu s$ has been determined.

In Fig. 20, a measurement of the demagnetizing interval is shown. The PWM signal is forced to zero, and a delay is inserted before the demagnetization process is started. After v_{demag} is set to zero (which opens the bidirectional switch S_2), the magnetizing current flows through the clamping diode and a CT voltage of $v_{CT} = -12$ V is measured during the demagnetization. After the CT is fully demagnetized, the magnetizing current and, therefore, the current through the clamping diode is zero, and the clamping diode will block. Since the output capacitances C_{OSS}

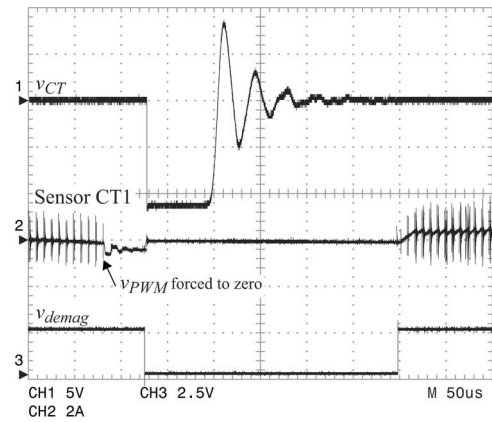


Fig. 20. CT voltage at demagnetization. After forcing the PWM signal to zero, the magnetizing current flows through the demagnetizing diode (CT voltage clamped to -12 V). After this current is zero, a resonant circuit is built by C_{OSS} of the bidirectional switch and L_m of the CT.

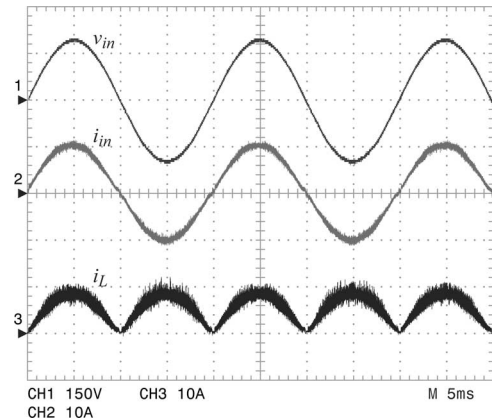


Fig. 21. Measurement results for the input voltage v_{in} , input current i_{in} , and inductor current i_L of the 1-kW PFC circuit. Sensor CT1 is used for current measurement for the current controller.

of the bidirectional switch are also charged to -12 V during the demagnetizing interval, again an oscillation occurs. Here, the resonant circuit is formed by L_m of the CT and C_{OSS} of the bidirectional switch. During this oscillation, the common source potential of the two MOSFETs can become negative, so that a negative gate voltage has to be applied to the bidirectional switch for ensuring a safe turn-OFF. The oscillations can be reduced by applying a MOSFET with a small output capacity C_{OSS} for the bidirectional switch. However, such MOSFETs usually show higher $R_{DS,ON}$ values contributing also to the total ohmic resistance of the burden path. Also, the calculated amplitude error of (8) can be seen in Fig. 20, where the sensor output at the end of the period is slightly negative instead of zero. Finally, measurement results of the 1-kW PFC circuit (input current i_{in} , input voltage v_{in} , and inductor current i_L) are presented in Fig. 21, which show that the PFC operates very well with the proposed current sensor.

VII. CONCLUSION

In this paper, a new current sensor concept for measuring ac + dc currents, which have periodic zero crossings, for

example, given in PFC applications, has been analyzed in detail. The proposed sensor consists of a CT and an active demagnetizing circuit, which demagnetizes the core of the CT during the zero crossings of the current. Here, the measured current is clamped to zero for a short period of time, which coincides with the inherent zero crossing distortions of active PFC circuit, so that the THD of the controlled current is not deteriorated.

For validating the presented design equations and models, prototype systems utilizing either nanocrystalline or ferrite-core material have been built and the transfer functions have been measured. Here, a bandwidth from dc up to 20 MHz and measurement errors below 2% have been achieved with the nanocrystalline materials. The bandwidth of the ferrite prototype is limited to values below 5 MHz, and the resulting measurement error is relatively high (> 6%). Furthermore, the performance of the proposed sensor concept has been measured in a 1-kW single-phase PFC test system, which revealed a THD of 1.5%.

The design of the proposed sensor is quite simple, and the size of the CT can be reduced significantly if the frequency of the ac current increases, for example, in aircraft power systems.

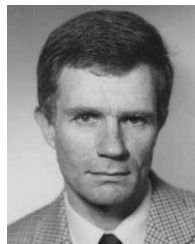
REFERENCES

- [1] J. W. Kolar and F. C. Zach, "A novel three-phase utility interface minimizing line current harmonics of high-power telecommunications rectifier modules," *IEEE Trans. Ind. Electron.*, vol. 44, no. 4, pp. 456–467, Aug. 1997.
- [2] T. Nussbaumer, M. Baumann, and J. W. Kolar, "Comprehensive design of a three-phase three-switch buck-type PWM rectifier," *IEEE Trans. Power Electron.*, vol. 22, no. 2, pp. 551–562, Mar. 2007.
- [3] K. Sangshin and H. A. Toliyat, "Design and rating comparisons of PWM voltage source rectifiers and active power filters for AC drives with unity power factor," *IEEE Trans. Power Electron.*, vol. 20, no. 5, pp. 1133–1142, Sep. 2005.
- [4] F. Blaabjerg, Z. Chen, and S. B. Kjaer, "Power electronics as efficient interface in dispersed power generation systems," *IEEE Trans. Power Electron.*, vol. 19, no. 5, pp. 1184–1194, Sep. 2004.
- [5] J. M. Carrasco, L. G. Franquelo, J. T. Bialasiewicz, E. Galvan, R. C. P. Guisado, Ma. A. M. Prats, J. I. Leon, and N. Moreno-Alfonso, "Power-electronic systems for the grid integration of renewable energy sources: A survey," *IEEE Trans. Ind. Electron.*, vol. 53, no. 4, pp. 1002–1016, Jun. 2006.
- [6] J. W. Kolar, U. Drogenik, J. Biela, M. L. Heldwein, H. Ertl, T. Friedli, and S. D. Round, "PWM converter power density barriers," *IEEEJ*, vol. 34, no. 3, pp. 473–479, May/Jun. 1998.
- [7] T. Noguchi, H. Tomiki, S. Kondo, and I. Takahashi, "Direct power control of PWM converter without power-source voltage sensors," *IEEE Trans. Ind. Appl.*, vol. 34, no. 3, pp. 473–479, May/Jun. 1998.
- [8] M. P. Kazmierkowski and L. Malesani, "Current control techniques for three-phase voltage-source PWM converters: A survey," *IEEE Trans. Ind. Electron.*, vol. 45, no. 5, pp. 691–703, Oct. 1998.
- [9] L. Dalessandro, U. Drogenik, S. D. Round, and J. W. Kolar, "A novel hysteresis current control for three-phase three-level PWM rectifiers," in *Proc. 20th Annu. IEEE Appl. Power Electron. Conf. Expo. (APEC 2005)*, Mar. 6–10, vol. 1, pp. 501–507.
- [10] P. Athalye, D. Maksimovic, and R. Erickson, "High-performance front end converter for avionics applications," *IEEE Trans. Aerosp. Electron. Syst.*, vol. 39, no. 2, pp. 462–470, Apr. 2003.
- [11] A. Radun, "An alternative low-cost current-sensing scheme for high-current power electronics circuits," *IEEE Trans. Ind. Electron.*, vol. 42, no. 1, pp. 78–84, Feb. 1995.
- [12] W. F. Ray and C. R. Hewson, "High performance Rogowski current transducers," in *Proc. Conf. Rec. 35th IEEE Ind. Appl. Conf.*, 2000, vol. 5, pp. 3083–3090.
- [13] F. Costa, E. Laboure, F. Forest, and C. Gautier, "Wide bandwidth, large AC current probe for power electronics and EMI measurements," *IEEE Trans. Ind. Electron.*, vol. 44, no. 4, pp. 502–511, Aug. 1997.
- [14] M. Hartmann, A. Muesing, and J. W. Kolar, "Switching transient shaping of RF power MOSFETs for a 2.5 MHz, three-phase PFC," in *Proc. 7th Int. Conf. Power Electron. (ICPE 2007)*, Oct. 22–25, pp. 1160–1166.
- [15] E. Laboure, F. Costa, and F. Forest, "Current measurement in static converters and realization of a high frequency passive current probe (50 A–300 MHz)," in *Proc. 5th Eur. Conf. Power Electron. Appl.*, 1993, Sep. 13–16, vol. 4, pp. 478–483.
- [16] A. Papp and H. Harms, "Magneto-optical current transformer. 1: Principles, 2: Components, 3: Measurements," *Appl. Opt.*, vol. 19, pp. 3729–3745, 1980.
- [17] A. P. Friedrich and J. Kunze, *Universal Magneto-resistive Current Sensor for Automotive Applications*. Wetzlar-Blankenfeld, Germany: SENSITEC GmbH, Im Amtmann 6, 6330.
- [18] G. Laimer and J. W. Kolar, "Design and experimental analysis of a DC to 1 MHz closed loop magneto-resistive current sensor," in *Proc. 20th Annu. IEEE Appl. Power Electron. Conf. Expo. (APEC 2005)*, Mar. 6–10, vol. 2, pp. 1288–1292.
- [19] L. Dalessandro, N. Karrer, and J. W. Kolar, "High-performance planar isolated current sensor for power electronics applications," *IEEE Trans. Power Electron.*, vol. 22, no. 5, pp. 1682–1692, Sep. 2007.
- [20] N. Karrer and P. Hofer-Noser, "A new current measuring principle for power electronic applications," in *Proc. 11th Int. Symp. Power Semicon. Devices ICs, (ISPSD 1999)*, pp. 279–282.
- [21] L.-L. Lee and C.-L. E. Tasy, "Novel zero ripple DC current transformer design," *IEEE Trans. Magn.*, vol. 35, no. 5, pp. 3514–3516, Sep. 1999.
- [22] I. M. Filanovsky and V. A. Piskarev, "Sensing and measurement of DC current using a transformer and RL-multivibrator," *IEEE Trans. Circuits Syst.*, vol. 38, no. 11, pp. 1366–1370, Nov. 1991.
- [23] L. Ghislanzoni and J. A. Carrasco, "A DC current transformer for large bandwidth and high common-mode rejection," *IEEE Trans. Ind. Electron.*, vol. 46, no. 3, pp. 631–636, Jun. 1999.
- [24] D. Slomovitz, "Electronic error reduction system for clamp-on probes and measuring current transformers," *IEEE Trans. Instrum. Meas.*, vol. 49, no. 6, pp. 1278–1281, Dec. 2000.
- [25] R. W. Erickson and D. Maksimovic, *Fundamentals of Power Electronics*, 2nd ed. New York: Springer-Verlag, 2001, pp. 181–182.
- [26] N. McNeill, N. K. Gupta, and W. G. Armstrong, "Active current transformer circuits for low distortion sensing in switched mode power converters," *IEEE Trans. Power Electron.*, vol. 19, no. 4, pp. 908–917, Jul. 2004.
- [27] N. McNeill, "Application of reset voltage feedback for droop minimization in the unidirectional current pulse transformer," *IEEE Trans. Power Electron.*, vol. 23, no. 2, pp. 591–599, Mar. 2008.
- [28] K.-W. Ma and Y.-S. Lee, "Technique for sensing inductor and DC output currents of PWM DC–DC converter," *IEEE Trans. Power Electron.*, vol. 9, no. 3, pp. 346–354, May 1994.
- [29] J. Sun, "On the zero-crossing distortion in single-phase PFC converters," *IEEE Trans. Power Electron.*, vol. 19, no. 3, pp. 685–692, May 2004.
- [30] Y.-K. Lo, S.-Y. Ou, and H.-J. Chiu, "On evaluating the current distortion of the single-phase switch-mode rectifiers with current slope maps," *IEEE Trans. Ind. Electron.*, vol. 49, no. 5, pp. 1128–1137, Oct. 2002.
- [31] J. P. Noon and D. Dalal, "Practical design issues for PFC circuits," in *Proc. 12th Annu. IEEE Appl. Power Electron. Conf. Expo. (APEC 1997)*, Feb. 23–27, vol. 1, pp. 51–58.
- [32] J. Biela and J. W. Kolar, "Using transformer parasitics for resonant converters—A review of the calculation of the stray capacitance of transformers," *IEEE Trans. Ind. Appl.*, vol. 44, no. 1, pp. 223–233, Jan./Feb. 2008.
- [33] L. Dalessandro, W. G. H. Odenaal, and J. W. Kolar, "HF characterization and nonlinear modeling of a gapped toroidal magnetic structure," *IEEE Trans. Power Electron.*, vol. 21, no. 5, pp. 1167–1175, Sep. 2006.
- [34] P. Poulichet, F. Costa, and E. Laboure, "High-frequency modeling of a current transformer by finite-element simulation," *IEEE Trans. Magn.*, vol. 39, no. 2, pp. 998–1007, Mar. 2003.
- [35] A. Massarini and M. K. Kazimierczuk, "Self-capacitance of inductors," *IEEE Trans. Power Electron.*, vol. 12, no. 4, Jul. 1997, pp. 671–676.
- [36] Vacuumschmelze. (2008). Datasheet of the AC-current sensor ZKB 564/401-80 [Online]. Available: www.vacuumschmelze.de
- [37] Omicron electronics. (2008). Handbook of the network vector analyzer: Bode100 [Online]. Available: www.omicron-labs.com
- [38] Tektronix. (2008). Instructions, A6302 & A6302XL 20 Ampere AC/DC current probes [Online]. Available: www.tektronix.com
- [39] Tektronix. (2008). Instructions, AM 503B, AM 5030 & A6300 series 067-0271-00 verification and adjustment kit [Online]. Available: www.tektronix.com



Michael Hartmann (S'08) received the B.S. (with honors) and M.Sc. (with honors) degrees in electrical engineering from the University of Technology Vienna, Vienna, Austria, in 2005 and 2006, respectively. He is currently working toward the Ph.D. degree at the Power Electronic Systems Laboratory, Swiss Federal Institute of Technology, Zurich, Switzerland, where he is engaged in active three phase rectifiers with ultrahigh switching frequencies.

He was engaged in switched-mode power amplifiers using multicell topologies. His current research interests include active three-phase rectifiers with ultrahigh switching frequencies.



Hans Ertl (M'93) received the Dipl.Ing. (M.Sc.) and the Ph.D. degrees in industrial electronics from the University of Technology Vienna, Vienna, Austria, in 1984 and 1991, respectively.

Since 1984, he has been with the University of Technology Vienna, where he is currently an Associate Professor in the Power Electronics Section, Institute of Electrical Drives and Machines. He has been engaged in numerous industrial and scientific research projects in the areas of field-oriented control of ac-drive systems, switch-mode power supplies for welding and industrial plasma processes, and active rectifier systems. He has authored or coauthored numerous scientific papers and patents. His current research interests include switch-mode power amplifiers and multicell topologies, in particular, for the generation of testing signals, for active ripple current compensators, and for several applications in the area of renewable energy systems.



Juergen Biela (S'04–M'08) received the degree in electrical engineering and the diploma (with honors) in October 2000 from Friedrich-Alexander University (FAU), Erlangen, Germany, and the Ph.D. degree from the Power Electronic Systems Laboratory (PES), Eidgenossische Technische Hochschule (ETH) Zurich, Zurich, Switzerland.

He was with Strathclyde University, Scotland, where he was engaged in resonant dc-link inverters. He was with the Technical University of Munich, Germany, where he was involved in the active control of series-connected integrated gate commutated thyristors (IGCTs). He was with the Research Department, A&D Siemens, Germany, where he was involved in inverters with very high switching frequencies, semiconductor (SiC) components, and electromagnetic compatibility (EMC). During 2006, he was a Guest Researcher at the Akagi/Fujita laboratory, Tokyo Institute of Technology, for three months. He is currently a Research Associate at the PES. His current research interests include design, modeling, and optimization of power-factor-corrected PFC/dc–dc converters for future energy systems and the design of pulse power systems.



Johann W. Kolar (M'89–M'91–SM'04) received the Ph.D. degree (*summa cum laude*) in industrial electronics from the University of Technology Vienna, Vienna, Austria.

From 1984 to 2001, he was with the University of Technology Vienna, where he was engaged in research in close collaboration with the industry. Since February 2001, he has been a Professor and the Head of the Power Electronics Systems Laboratory, Swiss Federal Institute of Technology (ETH) Zurich, Zurich, Switzerland. He has proposed numerous novel converter topologies, e.g., the VIENNA rectifier and the three-phase ac–ac sparse matrix converter concept. He has authored or coauthored more than 200 scientific papers published in international journals and conference proceedings, and has filed more than 50 patents. His current research interests include ultracompact intelligent ac–ac and dc–dc converter modules employing latest power semiconductor (SiC) technology, novel concepts for cooling and active electromagnetic interference (EMI) filtering, multidisciplinary simulation, bearingless motors, power microelectromechanical system (MEMS), and wireless power transmission.